J. Fluid Mech. (1995), *vol.* 288, *pp.* 37–58

Investigation of the effects of a compliant surface on boundary-layer stability

By T. LEE, M. FISHER AND W. H. SCHWARZ
Johns Hopkins University, Baltimore, MD 21218, USA

(Received 19 July 1993 and in revised form 3 June 1994)

Some of the effects of a passive, single-layer, viscoelastic compliant surface on the stability of a Blasius boundary layer were investigated in a low-turbulence wind tunnel. Measurements of the wavelength and growth rates of vibrating-ribbon-excited harmonic waves were made by hot-wire anemometry. The data for three compliant surfaces with different shear moduli, material damping coefficients, and thicknesses were compared to rigid-surface data. The flow-induced surface displacements were measured using an electro-optic displacement transducer. The results show that the growth rates of unstable Tollmien–Schlichting waves, and the extent of the unstable region in the (F, R_{δ^*})-plane are reduced over the compliant surfaces relative to those over a rigid surface with the absence of flow-induced surface instabilities. The suppression of the Tollmien–Schlichting waves is accompanied by a surface motion driven by the flow field at the excitation frequency. The experimental results suggest that a delay of the onset to turbulence is possible in air by using appropriately tuned surface characteristics. Further experiments are needed to study the three-dimensional disturbance mode, the flow-induced surface instabilities and the breakdown process.

1. Introduction

The stability of laminar shear flows and the transition to turbulence have received and continue to attract attention because of practical applications such as drag reduction. The concept of using a compliant coating to delay the laminar-to-turbulence transition of a boundary layer and to affect the turbulent boundary layer so as to produce a significant reduction in drag, was introduced by Kramer (1957). He suggested that the stability and transitional characteristics of the boundary layer may be influenced by the hydroelastic coupling to the compliant coating. The idea introduced by Kramer is very appealing if the fluid/solid interaction yields a net drag reduction.

A considerable amount of theoretical work (Benjamin 1960, 1963; Landahl 1962; Carpenter & Garrad 1985, 1986; Yeo 1986, 1988, 1990; Willis 1986; Sen & Arora 1988; Joslin & Morris 1989, 1992; Carpenter & Gajjar 1990; Carpenter & Morris 1990; Carpenter 1990; Carpenter, Lucey & Dixon 1991; Joslin, Morris & Carpenter 1991; Carpenter 1993; Dixon, Lucey & Carpenter 1994) has been done on the stability of a Blasius boundary layer using various models for the compliant surface. Also, there have been studies (Duncan, Waxman & Tulin 1985; Duncan 1986) of fully-developed turbulent boundary layers in order to understand the interaction of turbulence with the compliant coating. Experimental data (Blick & Walters 1968; Bushnell, Hefner & Ash 1977; McMichael, Klebanoff & Mease 1979; Gad-el-Hak, Blackwelder & Riley 1984; Riley, Gad-el-Hak & Metcalf 1988; Lee, Fisher & Schwarz 1993*a*) for turbulent boundary layers have been contradictory; some data support drag reduction (Blick &

Walters 1968) and other experiments do not (McMichael *et al.* 1979). The ambiguities are the result of the complexities of the boundary layer–compliant surface interaction.

Recent linear stability analyses of the Blasius boundary-layer flow over a compliant surface (Carpenter & Garrad 1985, 1986; Yeo 1986, 1988, 1990; Willis 1986; Sen & Arora 1988; Joslin & Morris 1989, 1992; Carpenter & Gajjar 1990; Carpenter 1990, 1993; Carpenter & Morris 1990; Carpenter *et al.* 1991; Joslin *et al.* 1991; Dixon *et al.* 1994) show that stabilization of the viscosity-induced Tollmien–Schlichting instability (TSI) waves can be achieved by the use of compliant coatings with appropriate compliance and material damping. However, since the compliant wall itself is also a wave-bearing medium, other possibly more dangerous flow-induced surface instabilities (FISI) can arise. These wall-based instabilities limit the transition-delaying performance of compliant surfaces. There are two main types of FISI: divergence, which is an essentially static instability, and travelling-wave flutter (see, for example, regimes B_1 and B_2, which correspond to the Class B instability of Benjamin (1963), in figure 5 of Yeo 1988). It is argued that the optimum compliant wall properties with respect to transition delay must be such that there is marginal stability with respect to both types of wall-based instabilities. A static-divergence instability (SDI) occurs when the conservative hydrodynamic pressure forces generated by a small disturbance outweigh the restorative structural forces in the wall. The appearance of SDI is always accompanied by an increase in turbulent viscous drag, which has been observed experimentally by Hansen & Hunston (1974, 1983), and Gad-el-Hak *et al.* (1984) in turbulent boundary-layer flows. Gad-el-Hak *et al.* (1984) also reported that SDI waves never appeared under a flat-plate laminar boundary layer with a free-stream velocity U_0 up to $12C_t$ (C_t is the shear-wave speed the material would have if there were no damping, which also represents the material stiffness of the surface; $C_t = (G'/\rho_s)^{1/2}$, where G' and ρ_s are the shear modulus and the density of the compliant material) over compliant coatings consisting of plastisol gels, while Hansen & Hunston (1983) observed a similar instability of a laminar boundary layer on a rotating coated disk at an onset speed of about $4.5C_t$. The travelling-wave flutter (TWF) instability mechanism involves the irreversible transfer of energy from the flow to the wall owing to the work done by the fluctuating pressure. TWF is responsible for the very sudden onset of transition. Furthermore, under certain circumstances, TSI and TWF can coalesce to form a powerful new instability (Carpenter & Garrad 1985; Yeo 1988) termed the transitional mode by Sen & Arora (1988). The transitional instability (see, for example, regime B_3 in figure 8 of Yeo 1988) causes a very rapid breakdown to turbulence. Both divergence and the transitional mode are absolute-type instabilities, whereas TWF, like TSI waves, is a convective-type instability. The identification of TWF and the transitional mode, and the practical realization of transition delay, based on the properties suggested by theoretical calculations for compliant walls, have become a major challenge to experimental investigators.

It is known that, in theory, TSI waves can be completely suppressed by using a sufficiently compliant wall, and what prevents this course of action from succeeding in practice is the appearance of FISI. Therefore, for successful stabilization, a compliant wall should have high flexibility and low damping to inhibit TSI waves. Also, the compliant material must not be so soft that a Kelvin–Helmholtz instability can occur. Further, the damping and shear modulus must be large enough to stabilize Class B (using the classification scheme of Benjamin 1960, 1963) flutter or free-wave modes. For systems that satisfy these criteria, a maximum increase in streamwise Reynolds number of 250% or 300% greater than that for a rigid wall has been predicted by Dixon *et al.* (1994) and Yeo (1986, 1988), respectively, for a Blasius boundary layer

over a single-layer, isotropic, viscoelastic compliant surface where the density ratio ($R_d = \rho_s/\rho_f$, where ρ_f is the density of the fluid) between the compliant material and the fluid is of order one. Also, for mathematical simplicity, the viscoelastic compliant layer was treated as a linear Voigt material of infinite horizontal extent that was bounded by a locally parallel basic flow field. No stability calculations for a compliant material have been reported for air where $R_d = 800$.

Several water-tunnel experiments have been carried out to study the effects of compliant walls on transition delay. Because the high background turbulence levels in the water tunnels caused premature transition at rather low speed, and also because of the lack of theoretical guidelines for the design of the compliant material, these experiments failed to report a delay in the transition. The only careful measurements of the growth of the flat-plate boundary layer instabilities over a compliant wall (where $R_d = 1$) were initiated by Gaster (1987) in a long towing tank using speeds of up to 3 m s^{-1}. Gaster's experiments were carried out with great care over four years to obtain the necessary low level of free-stream turbulence. The 45 cm × 45 cm compliant panel, located 30 cm downstream from the leading edge, was of a two-layer type, comprising a relatively thick and soft lower layer made of silicone rubber and a thin top layer made of a latex rubber membrane. The top layer was added originally for protection and ease of handling. Later, it was found that the addition of the stiff top layer had a beneficial effect on stability by restricting the tangential motion of the boundary (e.g. Yeo 1988; Dixon *et al.* 1994). The thickness of the compliant surface was 10 mm. Some of the properties of the compliant material (e.g. Young's modulus) are given in table 1 of Carpenter (1990). The forced two-dimensional waves were generated by periodically pumping minute quantities of fluid through an array of small holes in the plate surface ahead of the test panel, and were observed by using flush-mounted hot-film (FMHF) gauges on the rigid surface following the compliant section. Gaster's results show that (i) TSI waves do in fact suffer greatly reduced growth rate compared with similar waves in flow over a rigid plate; (ii) transition occurred at a speed 30% greater than that on a rigid panel; and (iii) the occurrence of fully turbulent flow seemed to be delayed to an even greater extent, provided that the unstable fluid/surface interaction modes (FISI) were avoided. There was also agreement between Willis' (1986) theoretical results and Gaster's experimental measurements that compliant walls, with the absence of FISI, can substantially reduce the growth of TSI waves. However, the amplification factors reported in Gaster's experiments were based on the ratio of the input excitation pressure to the fluctuating skin friction. The true amplitude of the wave at the excitation point was not known. Thus, there was an unknown constant of proportionality which had to be inferred by a comparison between experimental and theoretical amplification factors for the rigid wall. Also, because of the use of the FMHF gauges, Gaster was not able to measure (i) the disturbance at various streamwise locations along the compliant wall (i.e. the growth or decay of the TSI waves); and (ii) the distribution of disturbance velocity across the boundary layer. Furthermore, no information of the wall deformation was reported in Gaster's experiments.

It was our hypothesis that we could use a high air-flow speed to compensate for the very low density of air which then allowed us to systematically study the effects of a single-layer, isotropic, viscoelastic compliant surface on the stability of a laminar boundary layer in a low-turbulence wind tunnel. The objective of this experiment was to directly measure the behaviour of TSI waves on compliant surfaces with $R_d = 800$ for direct comparison with rigid surface measurements; not to focus on the changes in the transitional Reynolds number, or the reduction in drag. The growth and evolution

of the vibrating-ribbon-excited harmonic disturbance waves, the wavelength and wave speed, the distribution of disturbance velocity across the boundary layer, and the amplification rate over a compliant surface were examined by hot-wire anemometry and compared with those for the rigid-surface case at selected frequencies and free-stream velocities. Three viscoelastic compliant surfaces with different shear moduli, thicknesses, and damping coefficients were used to investigate the possible suppression of the TSI and/or FISI modes. A specially designed electro-optic surface displacement transducer was used to obtain the flow-induced surface displacements so as to better understand the interaction between a compliant surface and a Blasius flow.

2. Experimental apparatus and procedure

2.1. *Flow facility and test conditions*

Experiments were conducted in the low-turbulence Corrsin wind tunnel at The Johns Hopkins University. The closed-circuit tunnel has a 1 m × 1.2 m × 10.6 m test section with a contraction ratio of 25:1. The free-stream turbulence intensity is 0.04% at $U_0 = 25$ m s^{-1}. The test section has a built-in slow expansion to reduce the pressure gradient. The tunnel is equipped with a refrigeration unit that maintains the temperature of the air within ± 0.2 °F. An aluminium plate, 3.6 m long, 1.2 m wide and 2.5 cm thick, mounted horizontally along the centreline of the test section was used to obtain the Blasius boundary layer (see figure 1). The aluminium plate was spray-coated with an acrylic lacquer. The leading edge has an elliptic profile with a major-to-minor axis ratio of 8:1. A tail flap was used to position the stagnation point at the leading edge to prevent premature transition. The growth rates of the TSI disturbances over both rigid and compliant surfaces were measured over a range of non-dimensional ribbon excitation frequencies ($F = 2\pi\nu f/U_0^2 \times 10^6 = 55$–$250$, where ν is the kinematic viscosity of the fluid and f is the frequency) and flow speeds ($U_0 = 6$–24 m s^{-1}).

The basic state of the flat-plate experiment was established by verification of a near-zero pressure gradient and the determination of a high-transition streamwise Reynolds number, R_x^t, ($R_x^t = 2.58 \times 10^6$), and by surveys of the unexcited spanwise and traverse velocity distributions made at various locations to ensure that the developing boundary layer behaved as a Blasius-type flow. R_x^t was determined by both the impact-tube method (Schubauer & Skramstad 1947), and the fixed-velocity method (Reynolds & Saric 1986) at $U_0 = 18$ m s^{-1}. Figure 2 shows the change of the free-stream velocity along the flat plate. A variation of pressure was confined to the first 17 cm from the leading edge. Figure 3 shows the Blasius flow distributions at three different R_x ($R_x = xU_0/\nu$, where x is the distance downstream from the leading edge of the plate). The spanwise flow uniformity in the central test section was found to be within $\pm 1.5\%$. A least-squares approximation to the Blasius velocity profile shown in figure 3 obtained:

$$u(y)/U_0 = 1.71y/\delta \quad \text{for} \quad 0 < y/\delta < 0.182,$$
$$u(y)/U_0 = 1-(1.012-y/\delta)^2 \quad \text{for} \quad 0.182 < y/\delta < 1.012,$$

where $u(y)$ is the local mean velocity, and δ is the boundary-layer thickness. A detailed discussion of the difficulties and requirements for performing low-speed stability and transition experiments has been given by Saric (1990).

2.2. *Vibrating ribbon*

Two-dimensional harmonic waves were artificially introduced into the basic flow by the vibrating ribbon technique (Schubauer & Skramstad 1947; Klebanoff, Tidstrom & Sargent 1962; Nishioka, Iida & Ichikawa 1975; Kachnov & Levchenko 1984). A thin,

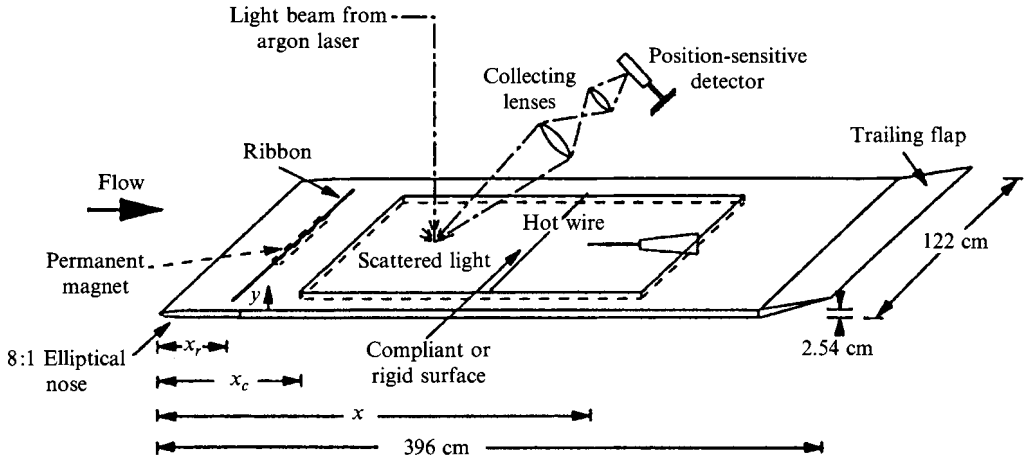

FIGURE 1. Schematic diagram of the experimental set-up.

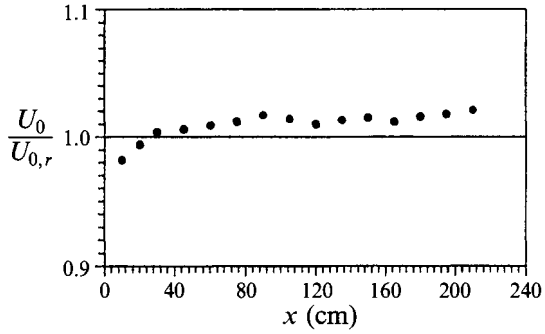

FIGURE 2. Free-stream velocity distribution along a rigid, flat plate. $U_{0,r}$ is the free-stream velocity approaching the leading edge of the plate.

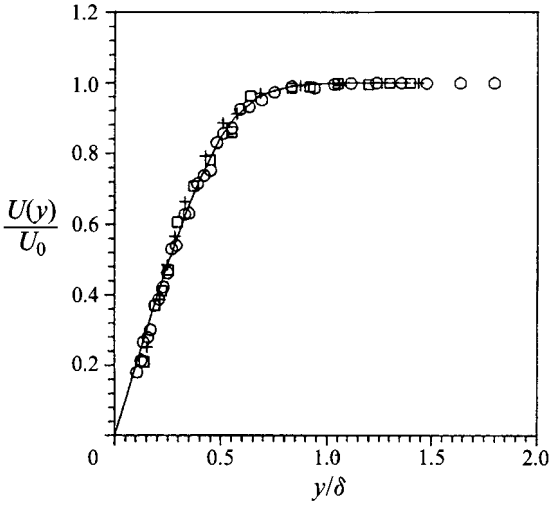

FIGURE 3. Mean-velocity distributions at various positions along a rigid, flat plate at $U_0 = 9.8$ m s^{-1}. ——, theoretical curve; present measurement: ○, $R_x = 3.794 \times 10^5$; □, $R_x = 7.587 \times 10^5$; +, $R_x = 9.484 \times 10^5$.

flat, phosphor-bronze ribbon (Surepure Chemetal Inc. model CDA510), 2.5 mm wide and 0.05 mm thick, was mounted spanwise on the plate at a height of 0.18 mm from the surface. The middle unsupported segment (30 cm long) of the ribbon was free to vibrate normal to the wall. A strip of Scotch tape was used to secure the rest of the ribbon to the plate. Tension was applied to the ribbon by using rubber bands. The ribbon was driven with a sinusoidal electric current in a steady magnetic field produced by permanent magnets mounted on the bottom side of the plate. The excitation current was supplied by a sine-wave generator passing through a power amplifier. The frequency, f, could be varied in a desired range. A bandpass filter (Rockland model 2342) was used to ensure that the a.c. current was free from both lower and higher harmonic contents. Frequency spectra of the output of the power amplifier were monitored using an FFT spectrum analyser (Ono-Sokki model CF-350). The amplitude of the vibration was proportional to the current. The measurements of the root-mean-square (r.m.s.) values of the amplitude were also made across the span of the ribbon to establish a test condition with negligible spanwise variation.

2.3. *Hot-wire measurements*

The fluctuations introduced into the boundary layer were measured by a hot-wire probe (DISA P11) with a constant-temperature anemometer (AA Lab AN-1003). The hot-wire signals were conditioned using a bandpass filter (Dytronic model 710) with a bandwidth of 1.5 Hz. The overheat ratio was set at 1.8. The hot-wire probe was mounted on a sting extended from a three-dimensional traversing mechanism. The hot wire was always oriented to pick up the x-component velocity. All measurements in the boundary layer were made 31 cm ahead of the carriage to avoid the local pressure field. Traverses were always made along the centreline of the plate. For most of the measurements, the hot wire was positioned at or near the location of the critical layer δ_c, where the wave matches the local mean velocity, in order to give maximum r.m.s.-amplitude measurements. This distance between the hot wire and the surface also eliminated the possible heat conduction loss to the conducting aluminium plate (Bhatia, Durst & Jovanovic 1982; Acharya & Escudier 1984; Krishnamoorthy, Wood, Atonia & Chambers 1985; Turan, Azad & Atamanchuk 1987).

All hot-wire calibrations, mean-flow measurements, free-stream turbulence levels, r.m.s.-disturbance (u') measurements, traverse control, and subsequent processing were performed on a Northgate 486 personal computer with a Computer Boards Cio-Das16/330 A/D converter board, using the Streamer data acquisition software. Waveforms and spectral analyses of u-component velocity fluctuations were made and recorded with an FFT spectrum analyser (Ono-Sokki model CF-350). The r.m.s. value of the u-fluctuations was also measured with an r.m.s. meter. The initial hot-wire location was measured using a cathetometer, based on the distance between the wire and its reflection from the surface. The calibration of the hot wire was carried out with a standard Pitot-static tube in connection with an electronic digital pressure transducer. The calibrations performed before and after each test run were reproduced to within 1.5% of each other. A fourth-order polynomial was fitted to the velocity-voltage calibration points using a least-squares approximation.

The wavelength, λ, was determined at constant U_0, f, and y by the Lissajou method. y is the distance of the hot wire above the surface. The input to the ribbon from the amplifier was connected to one of the channels in the oscilloscope and the output from the hot wire was connected to the other channel. The hot wire was traversed downstream from the ribbon for a streamwise distance of about 50 cm, and readings of x_l (x_l is the spacing for which the phase between the input of ribbon and output from

Compliant mix	G' (Pa)	η' (Pa s)	d (mm)	τ_t (s)	C_t (cm s^{-1})	x_c (cm)
9/91 (100)	230–270	25–35	5	10.43–13.48	48–52	60
10/90 (100)	310–360	60–90	10	10.78–15.0	55.7–60	60
10/90 (20)	310–360	15–22	6.3	4.28–5.82	55.7–60	45

10/90 (100) compliant mix indicates the compliant material was made by mixing 90% by weight of 100 mm^2 s^{-1} silicone oil with 10% of silicone elastomer. x_c indicates the leading edge of the compliant surface downstream from the leading edge of the plate.

TABLE 1. Surface characteristics of the three compliant surfaces tested

the hot-wire signal changed 180°) were made after each complete wavelength. The wave speed, C ($C = \lambda f$), was obtained by multiplying λ ($\lambda = 2x_l$) by f.

The growth or attenuation of a perturbation was determined by setting the ribbon into vibration at an arbitrarily fixed, small amplitude, and reading the r.m.s. hot-wire output voltage as the hot wire was moved away from the ribbon. The amplification coefficient β_i was obtained using the $\beta_i = 2.3Cd(\log_{10} u'/u'_0)/dx$ relation (Schubauer & Skramstad 1947). u'_0 is the u-component r.m.s. value at 5 cm downstream from the ribbon. The variation of the r.m.s. amplitude across the boundary layer was determined by traversing normal to the surface at selected distances behind the ribbon. Since the growth of the wave amplitude depends on the distance from the surface, it was critical to keep y constant as the hot wire was traversed downstream from the ribbon. In the present experiments, a constant y-location throughout the measurements was maintained by using the Blasius mean-velocity curve-fit equations and the hot-wire calibration polynomial together with the mean voltage output from the digital voltmeter of the anemometer test module. The determined y-value was also checked against the reading of the position of the hot wire using a cathetometer equipped with a calibrated graticule.

2.4. *Compliant materials*

The single-layer, passive, isotropic, viscoelastic compliant materials (Hess, Peattie & Schwarz 1993; Lee *et al.* 1993*a*, *b*) tested were made by mixing commercially available silicone elastomer (Dow-Corning Sylgard 184) and silicone oil (Dow-Corning series 200). The specific gravities for the elastomer and oil are 1.05 and 0.97, respectively. The amount and viscosity of the oil in the mixture can be varied to change the viscoelastic properties of the compliant material. The elastomer–oil mixture was poured into the 1 m × 1.8 m working section and cured at 175 °F. Three compliant surfaces with different shear moduli (G'), thicknesses (d), and material damping coefficients were tested in these experiments. The compliant properties are summarized in table 1. The low-frequency (0.006–1.0 Hz) complex modulus of the compliant mixture (G^*) was measured at The Johns Hopkins University with a Weissenberg rheogoniometer (model R18). Assuming that the parameters of a Voigt-solid model correspond to the average low-frequency values of the complex moduli, G_e (G_e is the shear modulus used in the Voigt-solid model) and η_v (η_v is the dynamic viscosity used in the Voigt-solid model), the damping coefficient τ_t ($\tau_t = \tau_r C_t/d$, where $\tau_r = \eta'/G'$ is the strain relaxation time, and η' is the dynamic viscosity which is the real part of the complex viscosity, η^*) can then be determined. However, C_t and τ_t depend on frequency for the complex viscoelastic material used in the present experiments. The frequency dependence of C_t and τ_t indicates that the Voigt model does not give an accurate representation of the viscoelastic material (see Appendix for details).

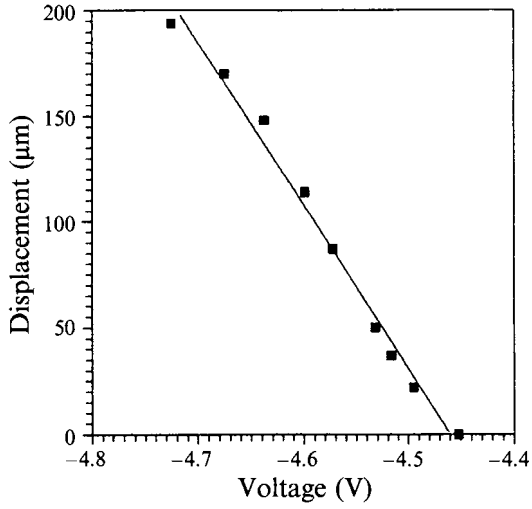

FIGURE 4. Typical surface displacement–transducer output voltage calibration curve.

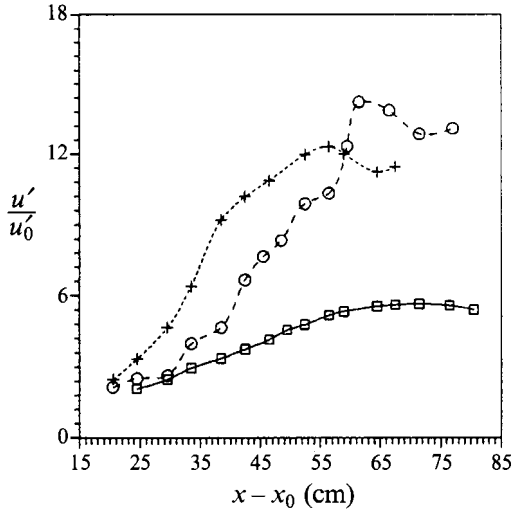

FIGURE 5. Root-mean-square-amplitude growth of the TSI at different initial amplitudes for $f =$ 96.5 Hz, $y = 1$ mm and $U_0 = 10.5$ m s^{-1}. □, $u'_0/U_0 = 0.11$; ○, $u'_0/U_0 = 0.5$; +, $u'_0/U_0 = 0.75$.

2.5. *Flow-induced surface displacement measurements*

A non-intrusive laser-based electro-optic transducer was utilized to measure the vertical component of the displacement of the compliant surface at selected points (see figure 1). The light beam from a 5 W argon laser was directed normal to the compliant surface. Incident light that scattered off the surface was collected by a two-lens combination, and was focused onto a positive-sensitive detector (Silicon Detector SD-1161-21-11-391). As the compliant surface displaces up and down, the spot image moves along the detector which causes a change in the detector output current and thereby allows the measurement of the vertical component of the motion. A specially designed electronic circuit was used to provide an output voltage linearly proportional to the position of the image on the active area of the detector. This voltage served as a measure of the displacement of the compliant surface from the undisturbed location

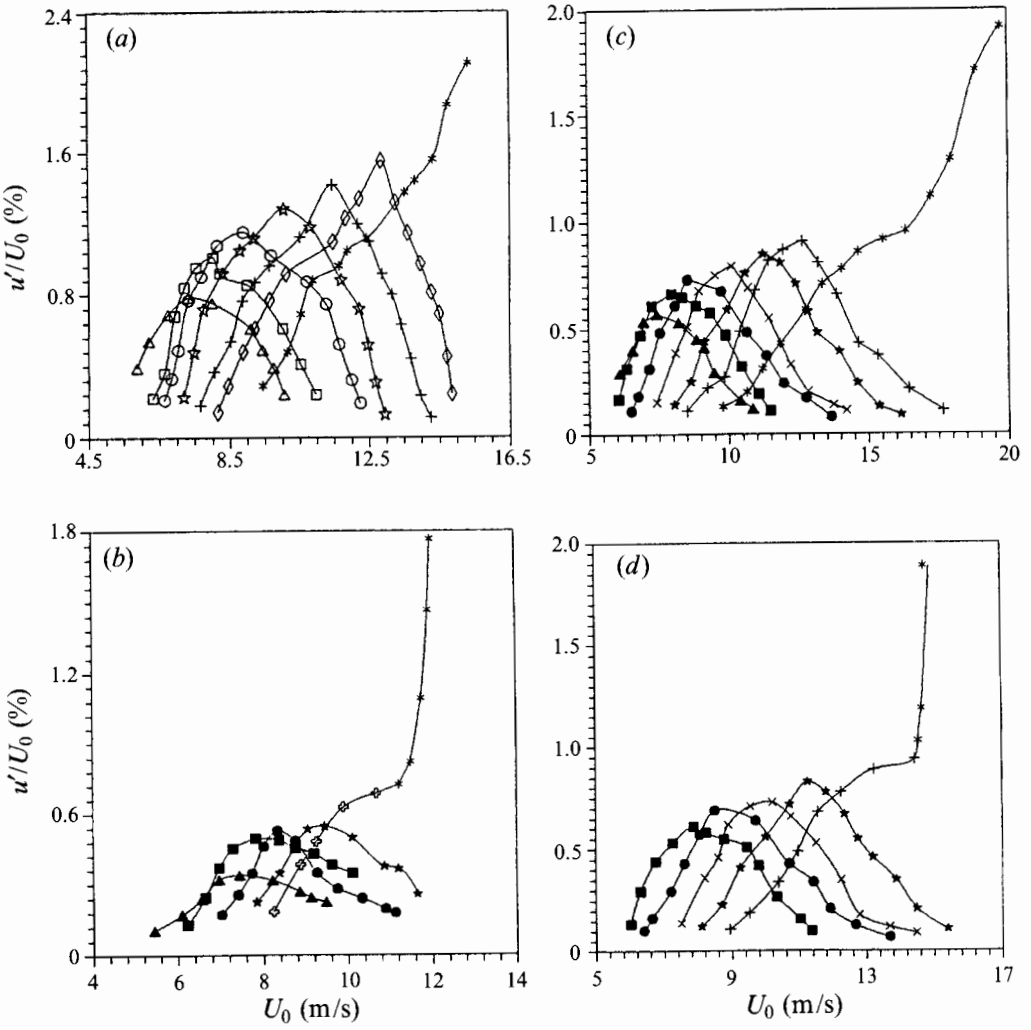

FIGURE 6. Disturbance r.m.s.-amplitude as a function of f and U_0 with x_r = 30 cm and x = 105 cm. (*a*) rigid surface: △, f = 54.8 Hz; □, f = 65.5 Hz; ○, f = 74.3 Hz; ☆, f = 84.8 Hz; +, f = 96.3 Hz; ◇, f = 105.3 Hz; *, f = 120.8 Hz, (*b*) 9/91–100 mm^2 s^{-1} oil compliant mix: ▲, f = 51.3 Hz; ■, f = 60.8 Hz; ●, f = 69.5 Hz; ★, f = 79.8 Hz; ✣, f = 84 Hz; *, f = 153 Hz, (*c*) 10/90–100 mm^2 s^{-1} oil compliant mix: ▲, f = 62 Hz; ■, f = 74.5 Hz; ●, f = 82.5 Hz; ×, f = 91 Hz; ★, f = 101 Hz; +, f = 114.5 Hz; *, f = 129 Hz, and (*d*) 10/90–20 mm^2 s^{-1} oil compliant mix: ■, f = 74 Hz; ●, f = 81 Hz; ×, f = 89 Hz; ★, f = 97.5 Hz; +, f = 103.5 Hz; *, f = 145.5 Hz.

through a calibration curve. Figure 4 shows a typical calibration curve for the output voltage from the surface-displacement transducer. The calibration was performed *in situ*. Details of the configuration and the electronic circuit are given in Hess *et al.* (1993).

3. Results and discussions

Figure 5 shows the growth of the r.m.s.-amplitude of the u-fluctuations, or the r.m.s.-disturbance, downstream from the vibrating ribbon over a rigid surface at three different initial amplitudes. The probe is located at y = 1 mm. At low initial amplitude

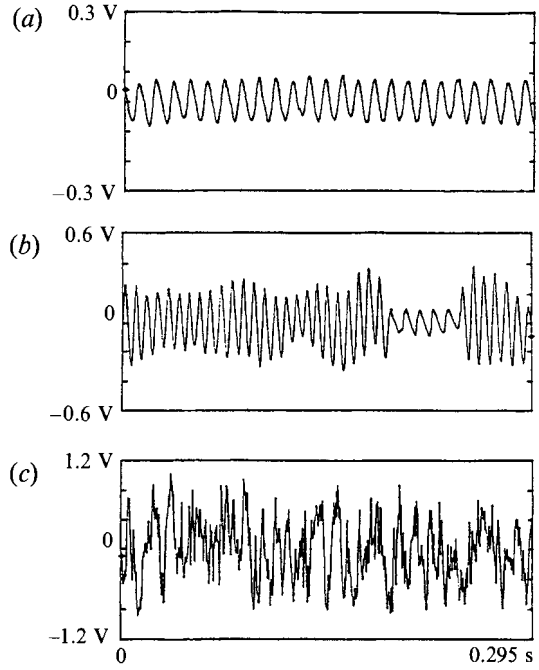

FIGURE 7. Wave patterns over 9/91–100 mm^2 s^{-1} oil compliant surface. (*a*) TSI wave patterns with $U_0 = 11.02$ m s^{-1} and $f = 84$ Hz; (*b*) FISI wave patterns with $U_0 = 11.31$ m s^{-1} and $f = 153$ Hz; and (*c*) turbulent flow with $U_0 = 11.58$ m s^{-1}.

($u_0'/U_0 = 0.11\%$), TSI waves grow and decay in the downstream direction as expected by the linear theory. For large amplitudes ($u_0'/U_0 = 0.5\%$ and 0.75%), the downstream development of the waves deviates from exponential growth, which is one of the characteristic features of the nonlinear development of large disturbances, and leads to the breakdown to transition (Klebanoff *et al.* 1962). In our experiments, sufficiently small amplitudes (but still much greater the natural background disturbances) were chosen to obtain a pure oscillation, and to ensure that the linearized theory would be satisfied.

Figure 6 shows the comparisons of the growth of the r.m.s.-disturbance over the three compliant surfaces to those of a rigid surface at different f and U_0. The ribbon was positioned at $x_r = 30$ cm. The probe was located 0.8 mm above the surface and 75 cm downstream from the ribbon. The disturbance is first seen to grow with U_0 and f, then decay if transition has not occurred in the unstable region. An r.m.s.-amplitude of the disturbance having lower values than those obtained for a rigid plate was recorded over the three compliant surfaces tested in the absence of FISI wave modes. Moreover, from the hot-wire signals and power spectra (see figure 7(*b*) for 9/91–100 mm^2 s^{-1} oil compliant mix), an unstable higher frequency (153 Hz) of the FISI wave or TWF was observed for $U_0 > 1.14$ m s^{-1} in addition to the corresponding primary frequency (84 Hz) of the TSI wave (see figure 7*a*) for the particular compliant material tested. Furthermore, with a slight increase in U_0, the amplitude grows rapidly and the flow become turbulent (see figure 7*c*). Figures 6(*b*) and 7(*b*) suggest that a detrimental transitional instability mode may be responsible for the rapid breakdown. Additional experimental studies are required to investigate the breakdown phenomenon and to identify other instability modes, such as TWF or the B_1 and B_2 regimes described by Yeo (1988). Figure 6(*c*) shows the effects of increased C_t, other

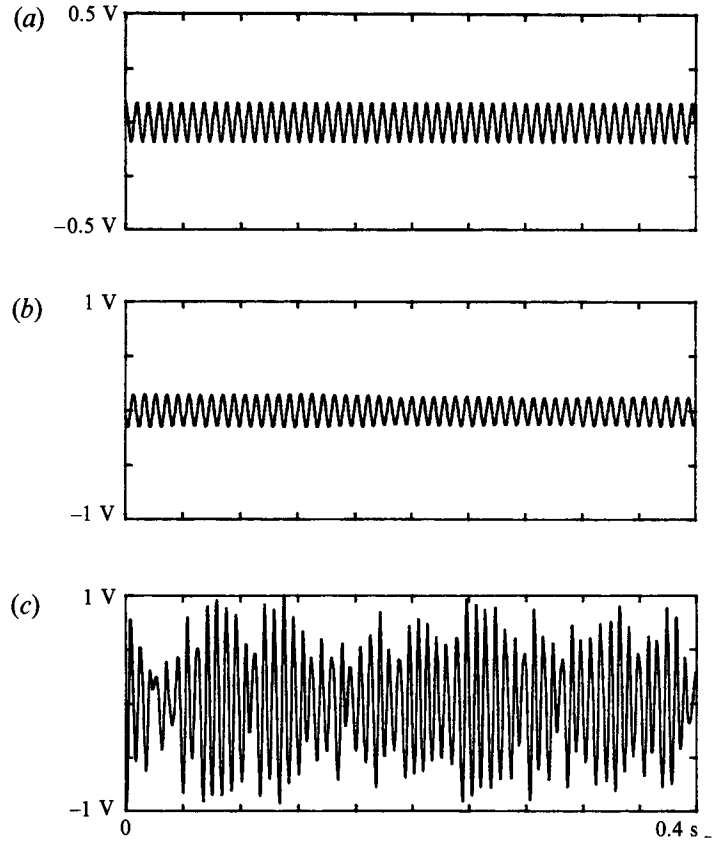

FIGURE 8. Wave patterns over 10/90–20 $mm^2\ s^{-1}$ oil compliant surface. (*a*) ribbon amplifier output; (*b*) TSI wave patterns with $U_0 = 14.5\ m\ s^{-1}$ and $f = 103.5$ Hz; and (*c*) FISI wave patterns with $U_0 = 14.71\ m\ s^{-1}$ and $f = 145.5$ Hz.

parameters being the same, on the destabilization of TSI and on the stabilization of FISI. A similar but reduced suppression in the r.m.s.-amplitude of the TSI for the 10/90–100 $mm^2\ s^{-1}$ oil compliant surface was found compared to that of a 9/91–100 $mm^2\ s^{-1}$ oil compliant mix (figure 6*b*); however, no FISI waves were observed. Figure 6(*d*) shows the effects of material damping coefficient on the unstable TSI and FISI waves. The results show that a decrease in surface damping coefficient has a strong promotive influence on the FISI mode (see also figure 8*c*), but a very mild stabilizing influence on TSI growth rates. Figure 6(*d*) also shows that an increase in shear modulus or C_t may also lead to a delay of the FISI to higher speed and frequency (compared to figure 6*b*).

Figure 8 shows the wave patterns over the 100/90–20 $mm^2\ s^{-1}$ oil compliant surface. Two-dimensional TSI waves were observed up to $U_0 = 14.5\ m\ s^{-1}$ at $f = 103.5$ Hz (see figure 8*b*). For $U_0 > 14.5\ m\ s^{-1}$, FISI waves appeared with $f = 145.5$ Hz (see figure 8*c*). The output from the ribbon amplifier is also shown in figure 8(*a*).

Figure 9 shows a typical comparison of the distribution of r.m.s.-amplitude of the disturbance across the boundary layer between the rigid and compliant surfaces. Figure 9(*a*), for the 9/91–100 mm^2/s^{-1} oil compliant surface, $U_0 = 10.12\ m\ s^{-1}$ and $F = 76.5$, indicates that there is a 40% reduction in the maximum r.m.s.-amplitude of the TSI wave disturbance under the influence of surface compliance, which may lead

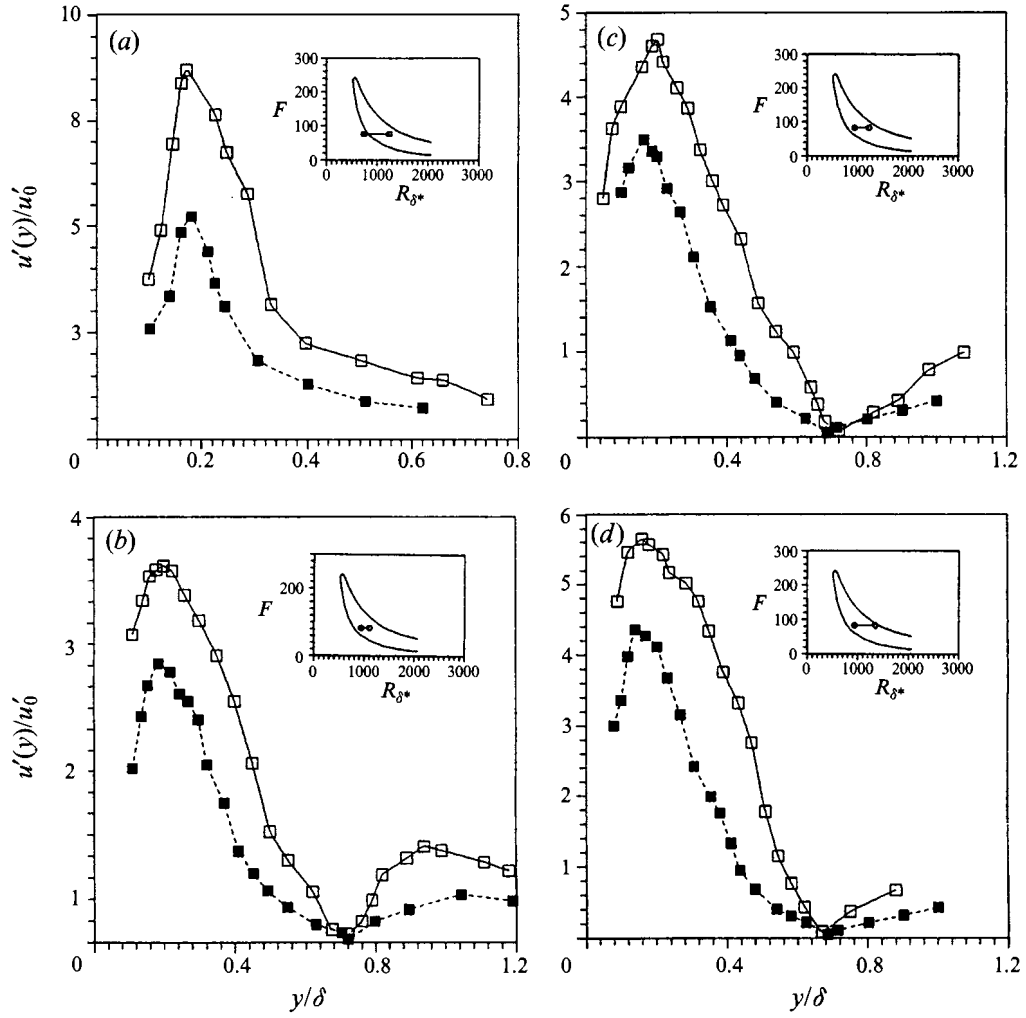

FIGURE 9. Comparison of distribution of r.m.s.-amplitude of the TSI of rigid surface and compliant surface across boundary layer. For 9/91–100 mm^2 s^{-1} oil compliant mix: (*a*) $R_{\delta^*} = 1274$, $U_0 = 10.12$ m s^{-1}, $F = 75.9$ and $x = 84$ cm. For 10/90–100 mm^2 s^{-1} oil mix, $U_0 = 8.9$ m s^{-1}, $F = 83.5$ and $x = 96$ cm; (*b*) $R_{\delta^*} = 1105$; (*c*) $R_{\delta^*} = 1225$; (*d*) $R_{\delta^*} = 1350$. □, rigid surface; ■, compliant surface. Inset shows locations of ribbon (solid symbol) and probe (open symbol) relative to neutral-stability curve.

to a delayed transition. Similar results were also found for the 10/90–100 mm^2 s^{-1} oil compliant surface at $R_{\delta^*} = 1105$, 1225 and 1350 with $U_0 = 8.9$ m s^{-1} and $F = 81.5$ (figures 9*b*, 9*c* and 9*d*). R_{δ^*} is the Reynolds number based on the boundary-layer displacement thickness (δ^*). These figures also show that the critical layer is a function of R_{δ^*} for both rigid and compliant surfaces. No measurable deviation from the Blasius mean-flow profile was observed for flows over compliant surfaces. A typical amplitude of the disturbance associated with the phase shift across the boundary layer at $R_{\delta^*} = 1105$ is shown in figure 10. The pairs of traces are simultaneous records of oscillations from the hot-wire (top), and the ribbon-amplifier output (bottom) at $y = 1$ mm. At the point within the boundary layer where u'/U_0 vanishes (see figure 10*g*), a 180° phase shift occurs in u', meaning that the instantaneous u-component of the oscillation

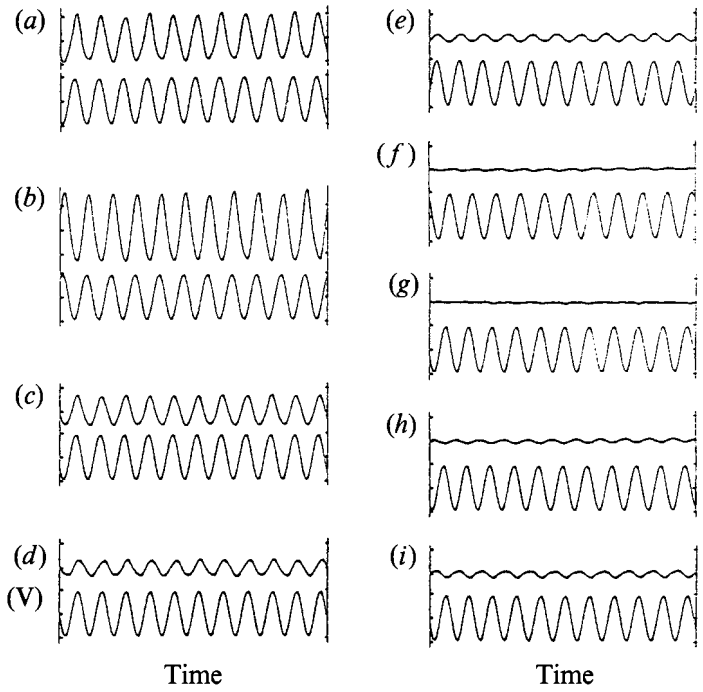

FIGURE 10. Oscillograms showing phase reversal in u-fluctuations for 10/90–100 mm^2 s^{-1} oil compliant surface. (*a*) $y/\delta = 0.14$; (*b*) $y/\delta = 0.18$; (*c*) $y/\delta = 0.32$; (*d*) $y/\delta = 0.4$; (*e*) $y/\delta = 0.55$; (*f*) $y/\delta = 0.68$; (*g*) $y/\delta = 0.72$; (*h*) $y/\delta = 0.8$; and (*i*) $y/\delta = 0.9$.

velocity is decreasing on one side of this point while increasing on the other. No significant departure of the 180° phase shift phenomenon from that of the rigid surface was observed except the differences in the peak r.m.s. value of u-fluctuations (u'_m) or δ_c and in the location of the phase shift (see figure 11). Also shown in this figure are the rigid-surface data of Ross *et al.* (1970) with $U_0 = 8.83$ m s^{-1} and $F = 82$. Figure 11 also shows that lower values of δ_c or u'_m were found for the 10/90–100 mm^2 s^{-1} oil compliant-surface case compared to those of the rigid surface.

Figure 12 shows the growth of the non-dimensional logarithmic value of $u'(x)/u'_I$ as a function of x for both the rigid and the 10/90–100 mm^2 s^{-1} oil compliant surfaces at different F with $U_0 = 8.5$ m s^{-1}, $x_r = 30$ cm and $y = 1$ mm. u'_I is the u-component r.m.s.-amplitude at branch *I*. $u'(x)$ is the r.m.s.-amplitude at streamwise location x. As the hot wire was moved downstream through the boundary layer, a regular oscillation appeared, weak at first but with increasing amplitude as the distance downstream increased. It appears that for both surfaces, whether a disturbance attenuates or grows while travelling downstream, the oscillation is strongly dependent on the ribbon vibration frequency and the free-stream velocity. Both a reduced r.m.s.-amplitude and amplification rate were observed with the presence of surface compliance compared to those of the rigid surface. The measurements of the growth of the two-dimensional disturbance (with $x_r = 55$ cm) in the streamwise direction also allow the determination of the x_{II} at branch *II* of the neutral stability curve. Similarly, the location of x_I at branch *I* was determined by positioning the ribbon at $x_r = 30$ cm. x_r is the ribbon location downstream from the leading edge of the plate. The total amplification of the disturbance and the points of neutral stability over both the rigid and compliant surfaces are shown in figures 13 and 14.

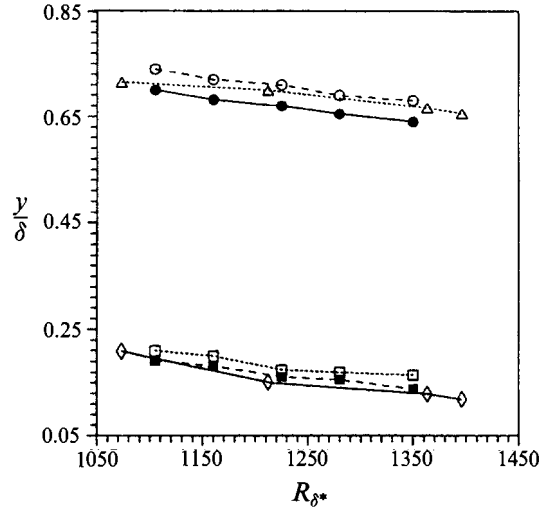

FIGURE 11. Comparison of the locations of peak r.m.s.-disturbance (i.e. δ_c) and the 180° phase shift of 10/90–100 mm^2/s^{-1} oil compliant surface with those of rigid surface at different R_{δ^*}. Measurements of δ_c: ◇, Ross *et al.* (1970); □, present rigid surface; ■, compliant surface. Measurements of the locations of 180° phase shift: △, Ross *et al.* (1970); ○, present rigid surface; ●, compliant surface.

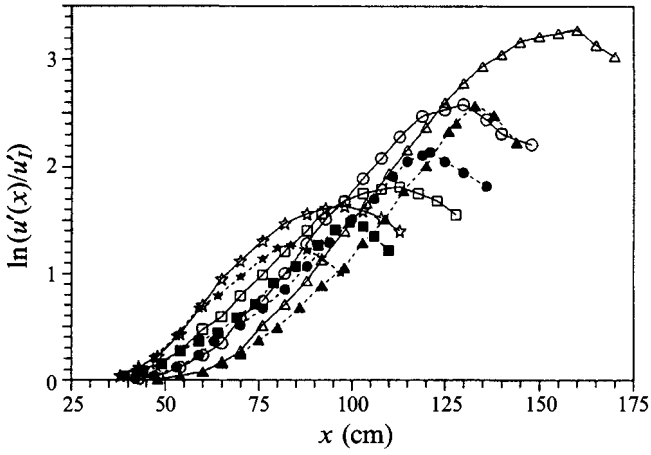

FIGURE 12. Comparison of the growth of r.m.s.-amplitude of the TSI of the 10/90–100 mm^2 s^{-1} oil compliant surface with those of rigid surface at different frequencies. Rigid-surface data: △, f = 70.5 Hz; ○, f = 76.5 Hz; □, f = 86.5 Hz; ☆, f = 93.5 Hz. Compliant-surface data: ▲, f = 70.5 Hz; ●, f = 76.5 Hz; ■, f = 86.5 Hz; ★, f = 93.5 Hz. $u'(x)$ is the local r.m.s.-value of u-fluctuations.

Figure 13 shows the amplification (u'_{II}/u'_c) of the two-dimensional disturbance travelling over the 9/91–100 mm^2 s^{-1} oil compliant surface compared to that of rigid surface at four different frequencies. The U_0 is 8.9 m s^{-1}. u'_c is the u-component r.m.s.-amplitude at the leading edge of the compliant surface. The figure shows that a 35% reduction in the amplification rate occurred over this particular compliant surface. Also shown in this figure are the total amplification (u'_{II}/u'_I) of the present rigid-surface measurements, which are consistent with those of Ross *et al.* (1970) and Schubauer & Skramstad (1947).

Figure 14 shows the measurements of the points at branches *I* and *II* of the neutral

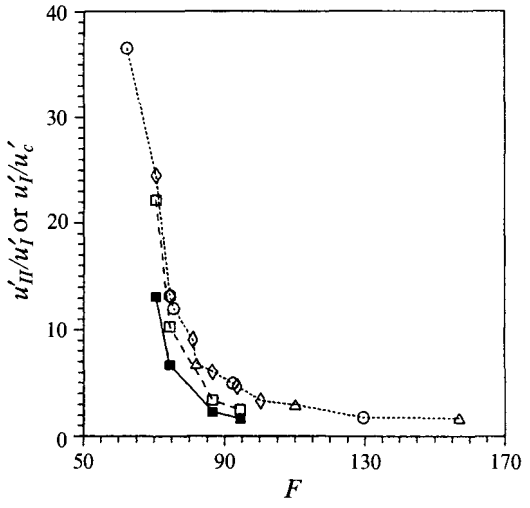

FIGURE 13. Amplification of r.m.s.-amplitude of the TSI as a function of F. Measurements of total amplification over rigid-surface measurement: ○, theoretical calculation by Schlichting in Schubauer & Skramstad 1947; △, Ross *et al.* 1970; ◇, present data. Partial amplification of the present measurements: □, rigid surface; ■, 10/90–100 mm^2 s^{-1} oil compliant surface.

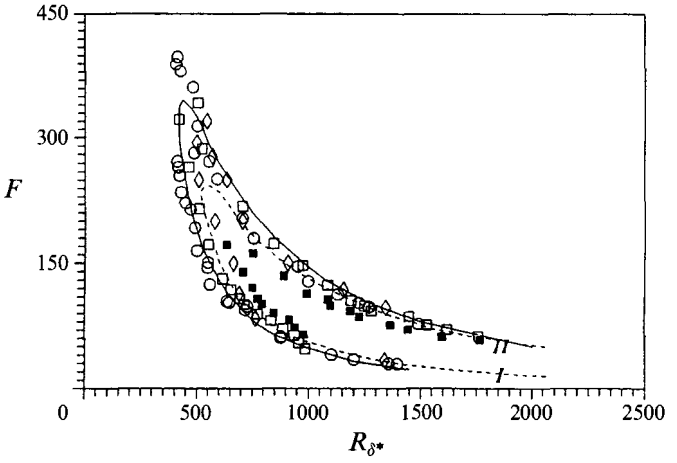

FIGURE 14. Comparison of neutral stability measurements of the present rigid and 10/90–100 mm^2 s^{-1} oil compliant surface with the published data. Rigid surface data: ——, non-parallel theoretical curve (Barry & Ross 1970); – – – –, parallel theoretical curve (Barry & Ross 1970); ◇, Schubauer & Skramstad 1947; ○, Ross *et al.* 1970; Present measurements: □, rigid surface; ■, compliant surface.

stability curve for both rigid and 10/90–100 mm^2 s^{-1} oil compliant surfaces in the (F, R_{δ^*})-plane. Branches *I* and *II* of the curve are represented, respectively, by the minima and maxima of u'. Downstream of branch *I*, the waves grow on a slow viscous scale and decay once they pass branch *II* of the neutral curve. The consistency of the present rigid-surface data (open squares) with published results (Schubauer & Skramstad 1947; Ross *et al.* 1970; Barry & Ross 1970) indicates that our small favourable pressure gradient test conditions (see figure 2) have a negligible stabilizing effect on the stability of the two-dimensional disturbance. This figure also shows that in addition to having

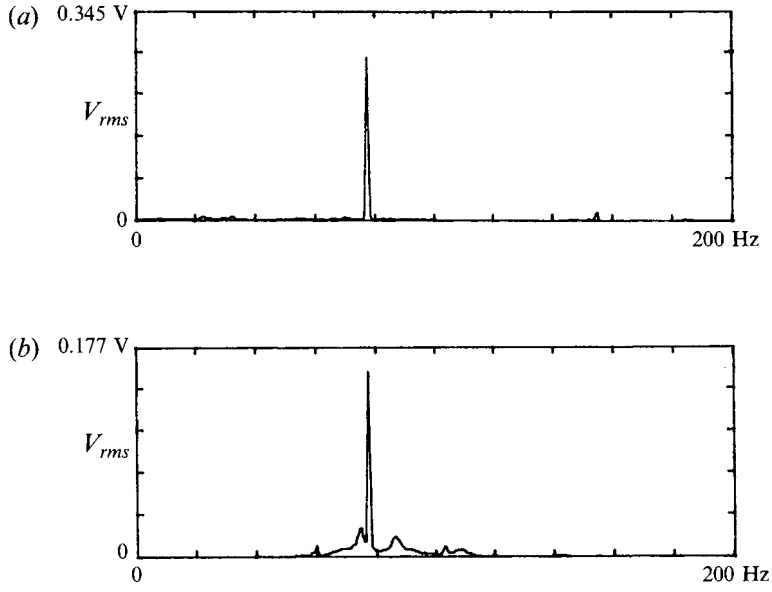

FIGURE 15. Spectra of u-fluctuations and surface undulations at $x = 96$ cm and $f = 77.5$ Hz for the 10/90–20 mm^2 s^{-1} oil compliant surface. (a) Hot-wire signals, and (b) surface-displacement signals.

Method A:	C (m s^{-1})		C/U_0		λ (cm)			
$\bar{R}_{\delta^*}$	S_R	S_C	S_R	S_C	S_R	S_C		
1105	3.19	2.92	0.358	0.328	4.91	4.49	—	—
1160	3.07	2.76	0.345	0.310	4.72	4.24	—	—
1225	2.67	2.47	0.300	0.278	4.12	3.80	—	—
1280	2.58	2.38	0.289	0.267	3.97	3.66	—	—
1350	2.51	2.11	0.282	0.237	3.87	3.25	—	—
Method B:	C (m s^{-1})		C/U_0		λ (cm)		β_i	
$\bar{R}_{\delta^*}$	S_R	S_C	S_R	S_C	S_R	S_C	S_R	S_C
1112	3.25	—	0.365	—	5.0	—	9.931	—
1110	—	2.93	—	0.329	—	4.5	—	8.924
1168	2.86	—	0.321	—	4.4	—	10.73	—
1165	—	2.60	—	0.292	—	4.0	—	8.302
1222	2.73	—	0.306	—	4.2	—	9.404	—
1227	—	2.47	—	0.277	—	3.8	—	7.011
1274	2.47	—	0.277	—	3.8	—	6.026	—
1282	—	2.34	—	0.263	—	3.6	—	3.978
1320	2.34	—	0.263	—	3.6	—	3.499	—
1325	—	2.15	—	0.242	—	3.3	—	1.784

Method A: C is determined using $u(y) = u(\delta_c)$ from figure 9.
Method B: λ is measured directly.
S_R indicates rigid surface.
S_C indicates compliant surface.
$\bar{R}_{\delta^*}$ is the mean Reynolds number at the beginning and end of the wavelength.

TABLE 2. Wave characteristics for the 10/90–100 mm^2 s^{-1} oil compliant surface with $U_0 = 8.9$ m s^{-1} and $f = 65$ Hz

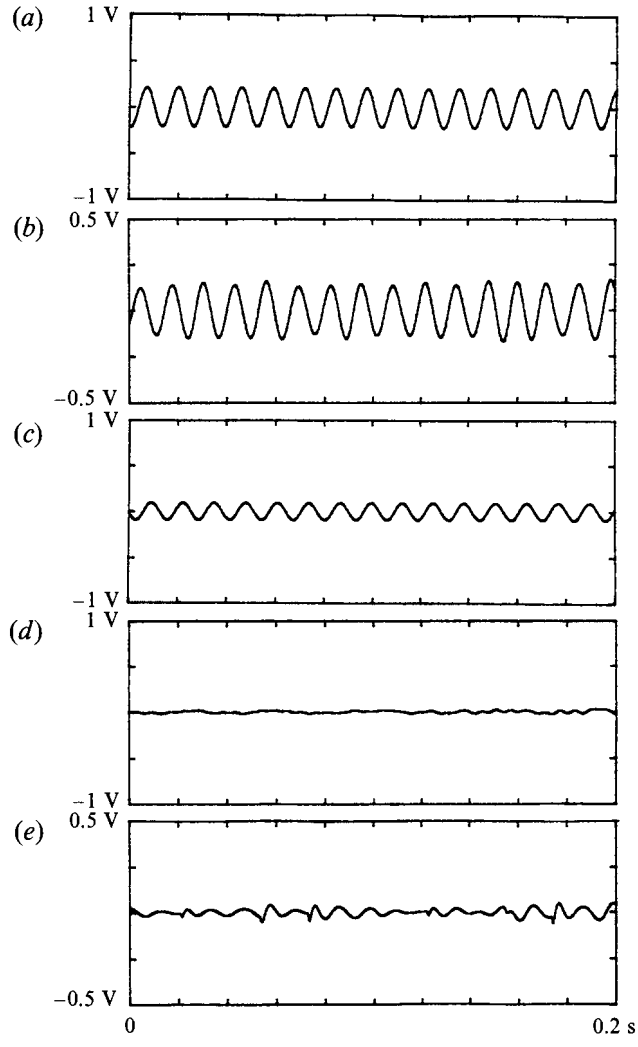

FIGURE 16. Wave forms of u-fluctuations and surface undulations at $x = 96$ cm and $f = 77.5$ Hz for the 10/90–20 mm^2 s^{-1} oil compliant surface. (*a*) Hot-wire signals, (*b*) surface displacement signals, and (*c*) ribbon amplifier output. (*d*) and (*e*) are the hot wire and displacement transducer outputs with $f = 0$ Hz.

a higher critical Reynolds number, at any given R_{δ^*}, the unstable region was narrowed for this particular compliant surface. The stabilizing phenomenon or the suppression of TSI waves under the influence of the compliant surface is consistent with the results shown in figures 6(*c*), 9, 12 and 13. This stabilizing effect was accompanied by lower values of wavelength, wave speed, and amplification coefficient (see table 2). It is worth noting that since the growth of boundary-layer thickness is a destabilizing influence, the increase of boundary-layer thickness with x may lead to an apparent amplification (Ross *et al.* 1970).

Figures 15(*a*) and 15(*b*) show typical power spectra of u-fluctuations and surface undulations at $x_r = 30$ cm, $x = 95$ cm and $f = 77.5$ Hz for 10/90–20 mm^2 s^{-1} oil compliant surface. The corresponding time-domain outputs are shown in figure 16. A phase difference of about 15° was found between the periodic velocity fluctuations and

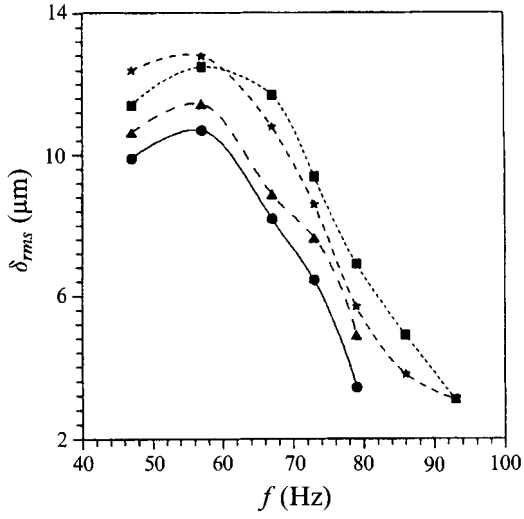

FIGURE 17. Root-mean-square-amplitude of the flow-induced surface displacement on the 10/90–100 mm^2 s^{-1} oil compliant surface at different f and U_0. ●, $U_0 = 8.5$ m s^{-1}; ▲, $U_0 = 9.6$ m s^{-1}; ★, $U_0 = 10.55$ m s^{-1}; ■, $U_0 = 12.5$ m s^{-1}.

surface undulations (see figures 16*a* and 16*b*). Also shown in figures 16(*d*) and 16(*e*) are the outputs from both the hot wire and the displacement transducer with $f = 0$ Hz, which give a reference of the magnitude of the natural boundary-layer oscillations and the surface undulations, respectively. All data were obtained at the centre of the compliant surface. The single-point displacement signals picked up by the electro-optic surface displacement transducer suggest that there is a stable interaction between the particular compliant surface and the Blasius boundary layer. Figures 15 and 16 also show that the suppression of the TSI waves is accompanied by a small-amplitude surface motion (figures 15*b* and 16*b*) driven by the flow field at the ribbon excitation frequency (figures 15*a* and 16*a*). Figure 17 shows the r.m.s. values of surface displacements at different f and U_0. The r.m.s.-surface displacements, δ_{rms}, were found to be a function of f at fixed U_0. δ_{rms} increases with increasing U_0 at constant f. These surface-displacement measurements also imply that this particular surface compliance may absorb energy from the basic flow and stabilize the TSI wave.

4. Conclusions

Some of the effects of a single-layer, viscoelastic compliant surface on the stability of a Blasius flow were studied in a low-turbulence wind tunnel. The growth and evolution of the vibrating-ribbon-excited harmonic waves were found to be suppressed, with the absence of FISI wave modes, for the three compliant surfaces tested. The results indicate that a delay of the onset of turbulence can be achieved by using appropriate material properties and thickness of the compliant surface.

We draw the following conclusions:

1. The growth and decay of the small disturbances on compliant surfaces, in the absence of FISI, behaves as predicted by linear theory.

2. The growth of the TSI waves and the extent of the unstable region in the (F, R_{δ^*})-plane of a compliant surface, in the absence of FISI, is reduced compared to those of a rigid surface.

3. Lower values of wave speed, wavelength, and amplification rate were found over the 10/90–100 $mm^2\ s^{-1}$ oil compliant surface compared to the rigid surface.

4. The suppression of the TSI waves is accompanied by a surface motion driven by the flow field at the excitation frequency.

5. The experimental results suggest that a delay of the onset of turbulence can be achieved in airflows provided that the very unstable fluid/surface interaction modes are avoided.

6. Further experiments should be undertaken to explore three-dimensional instability, which are more unstable than two-dimensional ones in laminar boundary-layer flows over compliant walls (Yeo 1988, 1990; Joslin *et al.* 1991), the TWF or FISI, and transitional instability modes, and the breakdown process.

7. Finally, theoretical calculations for $R_d = 800$ are needed to serve as a guideline for future experiments.

Portions of this work were performed with funding from the Office of Naval Research under contract number N00014-870K-0126. Also, we wish to acknowledge the support of the National Science Foundation for making the work on stability possible.

Appendix

Our compliant material consists of a silicone elastomer diluted with an inert silicone oil and is classified as a soft viscoelastic solid. Its rheological 'fingerprint' is complex. Generally, a nonlinear constitutive equation that represents the stress tensor as a functional of the history of the motion of the material is required for general deformations. However, if the displacements of material particles are small, then the constitutive equation for the stress can be represented by linear viscoelastic theory (Coleman & Noll, 1961). The stress tensor can be expressed by an equation of the form:

$$\boldsymbol{S}(t) = \boldsymbol{I}\left\{-p(\rho_{\mathscr{R}}) + 2\int_0^\infty tr[\boldsymbol{E}_{\mathscr{R}}(t-s) - \boldsymbol{E}_{\mathscr{R}}(t)]\, l(s,\rho_{\mathscr{R}})\,\mathrm{d}s\right\} + 2\int_0^\infty m(s,\rho_{\mathscr{R}})\,[\boldsymbol{E}_{\mathscr{R}}(t-s) - \boldsymbol{E}_{\mathscr{R}}(t)]\,\mathrm{d}s \quad \text{(A 1)}$$

where the subscript $\mathscr{R}$ refers to the reference state; t is the present time; and $s \equiv t-\tau$, where $\tau \leqslant t$ is a time in the past; $\boldsymbol{E}_{\mathscr{R}}$ is the infinitesimal strain tensor relative to the reference state; and $m(s;\rho_{\mathscr{R}})$ and $l(s;\rho_{\mathscr{R}})$ correspond to the scalar shear and compressional relaxation moduli, respectively. It is convenient to define the shear $\mu(s;\rho_{\mathscr{R}})$ and the compressional $\lambda(s:\rho_{\mathscr{R}})$ relaxation functions by:

$$m(s;\rho_{\mathscr{R}}) \equiv \frac{\mathrm{d}\mu(s;\rho_{\mathscr{R}})}{\mathrm{d}s}, \quad 2l(s;\rho_{\mathscr{R}}) \equiv \frac{\mathrm{d}\lambda(s;\rho_{\mathscr{R}})}{\mathrm{d}s}, \quad \text{(A 2)}$$

and

$$\mu(\infty;\rho_{\mathscr{R}}) \equiv G_e, \quad \lambda(\infty;\rho_{\mathscr{R}}) \equiv 0. \quad \text{(A 3)}$$

If we subject the material to a small-amplitude pure shearing oscillation (isochoric), the shear stress is related to the one-dimensional strain by the complex-valued form:

$$S_{12}^* = G^*(\omega)\,\kappa^*, \quad \text{(A 4)}$$

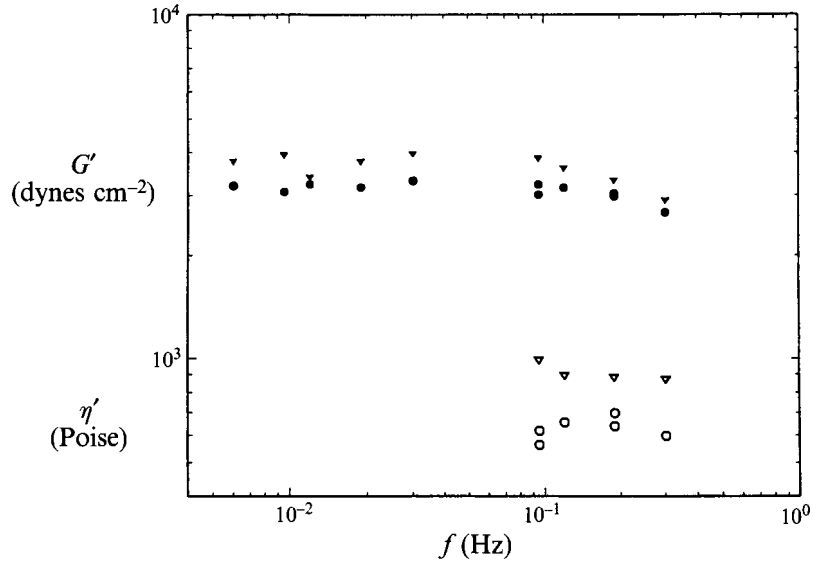

FIGURE 18. Shear storage modulus, G', and dynamic viscosity, η', as function of the frequency and age for the 10/90–100 mm^2 s^{-1} oil compliant surface. G': ●, 2 days; ▼, 5 days. η': ○, 2 days; ▽, 5 days.

where
$$G^* \equiv G' + \mathrm{i}G'' = \mathrm{i}\omega \int_0^\infty \mu(s;\rho_{\mathscr{R}})\, \mathrm{e}^{\mathrm{i}\omega s}\, \mathrm{d}s. \tag{A 5}$$

The complex shear modulus G^* is $\mathrm{i}\omega$ times the Fourier transform of the stress relaxation function. G' and G'' are called the storage and loss moduli, respectively. A fluid-like approach obtains the stress in terms of the rate-of-strain as:

$$S_{12}^* = \eta^* \dot{\kappa}^* = \eta^* \mathrm{i}\omega\kappa^*, \tag{A 6}$$

where η^* is the complex viscosity; $\dot{\kappa}$ is the rate of strain; and

$$G^* = \mathrm{i}\omega\eta^*. \tag{A 7}$$

Small-amplitude oscillatory deformations generated by a device such as the Weissenberg rheogoniometer (Walters 1975) are used to obtain G^* or η^*. The data are conveniently reported as a graph of G', the real part of the complex shear modulus, and η', the real part of the complex shear viscosity. These are indicators of the 'elastic' and 'viscous' components of the viscoelastic material. We remark that the compressional moduli require another type of measurement, e.g. by using acoustic waves (Schwarz 1975).

Data for the material used in these experiments are given in figure 18. These measurements and the data reported by Hess (1990), which were obtained for different elastomer–oil formulations, show that the compliant material for these experiments cannot be modelled precisely as a Voigt solid. This model of a spring and dashpot in parallel predicts that $G'(\omega) = G_e$ (a constant) and $\eta'(\omega) = \eta_V$ (a constant). The Voigt solid is considered to be too simplistic for viscoelastic materials (Ferry 1980). We note that in the low-frequency range (< 1 Hz), the values for G' and η' are relatively constant.

Figure 18 also indicates that the compliant material 'ages'; the complex moduli change with respect to time. For our material, the moduli change by about 10% in a five-day period.

REFERENCES

ACHARYA, M. & ESCUDIER, M. P. 1984 A direct formulation of correlations for wall-proximity corrections of hot-wire measurements. *Exps Fluids* **2**, 125.

BARRY, M. D. J. & ROSS, M. A. S. 1970 The flat plate boundary layer. Part 2. The effect of increasing thickness on stability. *J. Fluid Mech.* **4**, 813.

BENJAMIN, T. B. 1960 Effects of a flexible surface on hydrodynamic stability. *J. Fluid Mech.* **6**, 513.

BENJAMIN, T. B. 1963 The threefold classification of unstable disturbances in flexible surfaces bounding inviscid flows. *J. Fluid Mech.* **14**, 436.

BHATIA, J. C., DURST, F. & JOVANOVIC, J. 1982 Corrections of hot-wire anemometer measurements near walls. *J. Fluid Mech.* **122**, 411.

BLICK, F. B. & WALTERS, R. R. 1968 Turbulent boundary-layer characteristics of compliant surfaces. *J. Aircraft* **5**, 11.

BUSHNELL, D. M., HEFNER, J. N. & ASH, R. L. 1977 Effect of compliant wall motion on turbulent boundary layer. *Phys. Fluids* **20**, S31.

CARPENTER, P. W. 1990 Status of transition delay using compliant walls. In *Viscous Drag Reduction in Boundary Layer* (ed. D. Bushnell & J. J. Hefner), p. 79. AIAA.

CARPENTER, P. W. 1993 The optimization of multi-panel compliant walls for delay of laminar–turbulent transition. *AIAA J.* **31**, 1187.

CARPENTER, P. W. & GAJJAR, J. S. B. 1990 A general theory for two- and three-dimensional wall-mode instabilities in boundary layers over isotropic and anisotropic compliant walls. *Theoret. Comput. Fluid Dyn.* **1**, 349.

CARPENTER, P. W. & GARRAD, A. D. 1985 The hydrodynamic stability of flow over Kramer-type compliant surfaces. Part 1. Tollmien–Schlichting instabilities. *J. Fluid Mech.* **155**, 46.

CARPENTER, P. W. & GARRAD, A. D. 1986 The hydrodynamic stability of flow over Kramer-type compliant surfaces. Part 2. Flow-induced surface instabilities. *J. Fluid Mech.* **170**, 199.

CARPENTER, P. W., LUCEY, A. D. & DIXON, A. E. 1991 The optimization of compliant walls for drag reduction. In *Recent Development in Turbulence Management* (ed. K.-S. Choi), p. 223. Kluwer.

CARPENTER, P. W. & MORRIS, P. J. 1990 The effect of anisotropic wall compliance on boundary-layer stability and transition. *J. Fluid Mech.* **218**, 171.

COLEMAN, B. D. & NOLL, W. 1961 Foundations of linear viscoelasticity. *Rev. Mod. Phys.* **33**, 239.

DIXON, A. E., LUCEY, A. D. & CARPENTER, P. W. 1994 Optimization of viscoelastic compliant walls for transition delay. *AIAA J.* **32**, 256.

DUNCAN, J. H. 1986 The response of an incompressible, viscoelastic coating to pressure fluctuations in a turbulent boundary layer. *J. Fluid Mech.* **171**, 339.

DUNCAN, J. H., WAXMAN, A. M. & TULIN, M. P. 1985 The dynamics of waves at the interface between a viscoelastic coating and a fluid flow. *J. Fluid Mech.* **158**, 177.

FERRY, J. D. 1980 *Viscoelastic Properties of Polymers.* John Wiley.

GAD-EL-HAK, M., BLACKWELDER, R. F. & RILEY, J. J. 1984 On the interaction of compliant coatings with boundary-layer flows. *J. Fluid Mech.* **140**, 257.

GASTER, M. 1987 Is the dolphin a red herring? In *IUTAM Symp. Turbulence Management and Relaminarization* (ed. H. W. Liepmann & R. Narashima), p. 285.

HANSEN, R. J. & HUNSTON, D. L. 1974 An experimental study of turbulent flows over compliant surfaces. *J. Sound Vib.* **34**, 297.

HANSEN, R. J. & HUNSTON, D. L. 1983 Fluid-property effects on flow-generated waves on a compliant surface. *J. Fluid Mech.* **133**, 161.

HESS, D. E. 1990 An experimental investigation of a compliant surface beneath a turbulent boundary layer. PhD dissertation, The Johns Hopkins University.

HESS, D. E., PEATTIE, R. A. & SCHWARZ, W. H. 1993 A noninvasive method for the measurement of flow-induced surface displacement of a compliant surface. *Exps Fluids* **14**, 78.

JOSLIN, R. D. & MORRIS, P. J. 1989 The sensitivity of flow and surface instabilities to changes in compliant wall properties. *J. Fluids Struct.* **3**, 423.

JOSLIN, R. D. & MORRIS, P. J. 1992 Effect of compliant walls on secondary instability in boundary-layer transition. *AIAA J.* **30**, 332.

JOSLIN, R. D., MORRIS, P. J. & CARPENTER, P. W. 1991 Role of three-dimensional instability in compliant wall boundary-layer transition. *AIAA J.* **29**, 1603.

KACHNOV, YU. S. & LEVCHENKO, V. YA 1984 The resonant interaction of disturbances at laminar–turbulent transition in a boundary layer. *J. Fluid Mech.* **138**, 209.

KLEBANOFF, P. S., TIDSTROM, K. D. & SARGENT, L. M. 1962 The three-dimensional nature of boundary-layer instability. *J. Fluid Mech.* **12**, 1.

KRAMER, M. O. 1957 Boundary-layer stabilization by distributed damping. *J. Aero. Sci.* **24**, 459.

KRISHNAMOORTHY, L. V., WOOD, D. H., ANTONIA, R. A. & CHAMBERS, A. J. 1985 Effect of wire diameter and overheat ratio near a conducting wall. *Exps Fluids* **3**, 121.

LANDAHL, M. T. 1962 On the stability of a laminar incompressible boundary layer over a flexible surface. *J. Fluid Mech.* **13**, 609.

LEE, T., FISHER, M. & SCHWARZ, W. H. 1993*a* Investigation of the stable interaction of a passive compliant surface with a turbulent boundary layer. *J. Fluid Mech.* **257**, 373.

LEE, T., FISHER, M. & SCHWARZ, W. H. 1993*b* The measurement of flow-induced surface displacement on a complaint surface by optical holographic interferometry. *Exps Fluids* **14**, 158.

MCMICHAEL, J. M., KLEBANOFF, P. S. & MEASE, N. 1979 Experimental investigation of drag on a compliant surface. In *Viscous Flow Drag Reduction* (ed. G. R. Hough), p. 410. AIAA.

NISHIOKA, M., IIDA, S. & ICHIKAWA, Y. 1975 An experimental investigation of the stability of plane Poiseuille flow. *J. Fluid Mech.* **72**, 731.

REYNOLDS, G. A. & SARIC, W. S. 1986 Experiments on the stability of the flat-plate boundary layer with suction. *AIAA J.* **24**, 202.

RILEY, J. J., GAD-EL-HAK, M. & METCALF, R. W. 1988 Compliant coatings. *Ann. Rev. Fluid Mech.* **20**, 393.

ROSS, J. A., BARNES, F. H., BURNS, J. G. & ROSS, M. A. S. 1970 The flat plate boundary layer. Part 3. Comparison of theory with experiment. *J. Fluid Mech.* **43**, 819.

SARIC, W. S. 1990 Low-speed experiments: requirements for stability measurements. In *Instability and Transition* (ed. M. Y. Hussain & R. G. Voigt), p. 162. Springer.

SCHUBAUER, G. B. & SKRAMSTAD, H. K. 1947 Laminar boundary-layer oscillations and transition on a flat plate. *NBS RP*1772.

SCHUSTER, H. H. 1972 An experimental study of the interaction between a highly compliant boundary and turbulent shear flow. PhD dissertation, The Johns Hopkins University.

SCHWARZ, W. H. 1975 Acoustic wave propagation in a viscoelastic fluid undergoing a simple steady shearing motion. *J. Acoust. Soc. Am.* **58**, 1196.

SEN, P. K. & ARORA, D. S. 1988 On the stability of laminar boundary-layer flow over a flat plate with a compliant surface. *J. Fluid Mech.* **197**, 201.

TURAN, O., AZAD, R. S. & ATAMANCHUK, T. M. 1987 Wall effects on the hot-wire signal without flow. *J. Phys.* E: *Sci. Instrum.* **20**, 1278.

WALTERS, K. 1975 *Rheometry*. Whitstable Litho.

WILLIS, G. J. K. 1986 Hydrodynamic stability of boundary layers over compliant surfaces. PhD thesis, University of Exeter.

YEO, K. S. 1986 The stability of flow over flexible surfaces. PhD thesis, University of Cambridge.

YEO, K. S. 1988 The stability of boundary-layer flow over single- and multi-layer viscoelastic walls. *J. Fluid Mech.* **196**, 359.

YEO, K. S. 1990 The hydrodynamic stability of boundary-layer flow over a class of anisotropic compliant walls. *J. Fluid Mech.* **220**, 125.